

REVIEW

Open Access



# Inductive coupling for wireless power transfer and near-field communication

Christoph Degen\*

\*Correspondence:  
christoph.degen@hs-  
niederrhein.de  
Faculty of Electrical  
Engineering and Computer  
Science, Hochschule  
Niederrhein – University  
of Applied Sciences,  
Reinarzstr. 49, 47805 Krefeld,  
Germany

## Abstract

This paper gives an overview of optimizing wireless power transfer systems using magnetic coupling. Optimization aims to maximize either the power transfer efficiency or the transferred power. The resulting load calculation and matching strategies are revisited. Moreover, the coupling system is described, starting with its equivalent circuit and scattering parameters. In addition to wireless power transfer, communication in RFID and NFC systems and its frequency characteristics and bandwidth issues are highlighted. The focus in this paper is on load modulation for data transfer between a tag and reader. For this purpose, subcarrier voltages are derived using time-domain as well as frequency-domain signal analysis.

**Keywords:** Wireless power transfer, Inductive/magnetic coupling, NFC, Scattering parameters, Load modulation

## 1 Introduction

This paper focuses on wireless power transfer (WPT) between two coils with inductive coupling, which is typically in the MHz frequency range. With frequencies of less than 100 kHz, this technology is usually referred to as inductive power transfer (IPT), as it is based on the principle of non-radiative near-field electromagnetic coupling. Many applications for this technology already exist, for example smartphone battery charging [1], biomedical implants, electric vehicles, consumer electronics and industrial applications [2, 3]. Optimization strategies for charging electric vehicles are presented in [2] and [4].

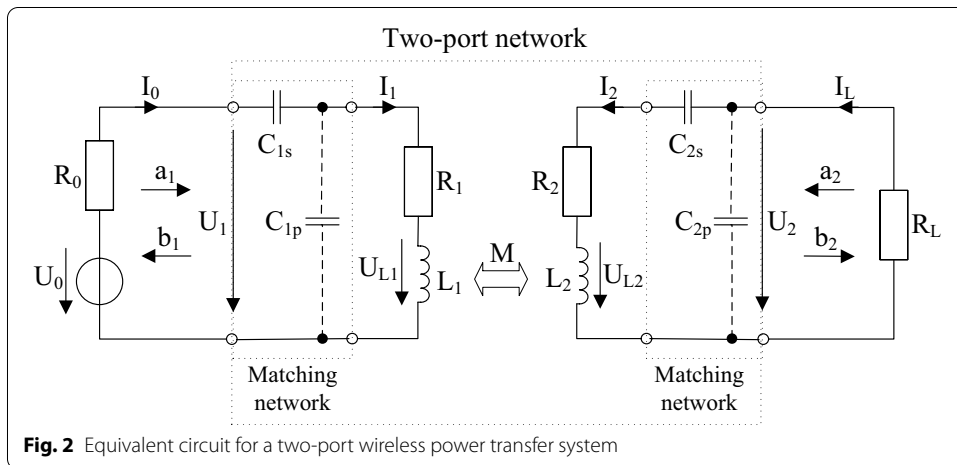
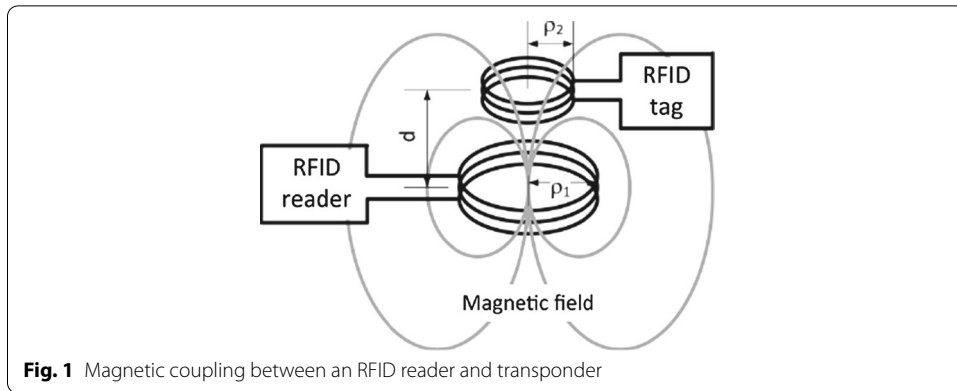
Wireless power transfer (WPT) for battery charging using inductive links at high frequency (HF) is being standardized by the Wireless Power Consortium for operating frequencies in the range of 87–205 kHz [5]. Depending on the application (tightly or loosely coupled systems, coil alignment tolerances, etc.), resonant or non-resonant inductive coupling is applied. In [6], the standardization effort focuses on magnetic resonant wireless power transfer at 6.78 MHz (the industrial, scientific and medical (ISM) band). Energy can also be harvested from existing ambient radio-frequency (RF) sources (cellular networks, WLAN, etc.). An overview of harvesting technologies for standalone wireless sensor platforms as well as aspects of realizing such technologies (available power, time for charging a storage device, etc.) is given in [7].

Passive radio-frequency identification (RFID) systems already carry out energy harvesting over a long time by exploiting energy from the reader RF signal. Near-field communication (NFC) offers battery-assisted as well as batteryless operation modes. In the batteryless mode, an NFC-enabled device harvests energy from incoming RF emission (from a reader) to power the sensor interface and RF transmission. In [8], an overview of NFC sensors for IoT applications is given, highlighting inductive coupling issues such as the quality factor and bandwidth. Moreover, detuning due to metallic surfaces is addressed there. A review of near-field wireless power transfer and communication with a focus on biomedical applications is given in [9]. NFC operates within the unlicensed radio-frequency ISM band of 13.56 MHz. In the passive (batteryless) mode, the NFC interface behaves similarly to an RFID system in which an NFC target, for example, transmits data by generating a *load modulation* and *modulated subcarrier* at a distance of  $\pm f_i$  to either side of the transmission frequency [10]. The subcarrier frequency is  $f_i = 847.5 \text{ kHz} (= 13.56 \text{ MHz}/16)$  in ISO/IEC 14443, with bit rates of 106–848 kbps. A combination of WPT and NFC with a focus on bandwidth, quality factor and a means for increasing bandwidth with an additional resistor was proposed in [11].

In this paper, optimization strategies for addressing power maximization and signal distortion issues during data transfer in communication mode are described using scattering parameters. A good description of general free-space propagation using scattering parameters can be found in [12], leading to a complex-valued Friis formula. This is of importance for communication between a transmitter and a receiver. For radar applications, the radar cross section (RCS) of a target is of interest, describing the relation between incoming power from the transmitter and power being reflected to the receiver. For RFID/NFC applications in the UHF band, the RCS is also of interest because a tag is handled as a radar target. For optimizing load modulation in such scenarios, complex-valued coupling between the RFID reader and tag, including a complex-valued RCS for the RFID tag, was introduced in [13].

The analysis of load modulation in this paper comprises time-domain as well as frequency-domain investigations. In particular, the scattering parameters are based on a single frequency in a steady-state scenario. Alternatively, the wavelet transform offers the possibility of time *and* frequency resolution [14–17]. Typical applications include signal analysis in volcanology [18], image dehazing and denoising [19], image classification [20] and document analysis [21]. Among the different wavelet functions that have been proposed, Morse and Morlet wavelets are examined in [22]. They are well-suited for time localization, which could be applied here to evaluate the switching times during load modulation but is beyond the scope of this paper. Moreover, fractal geometries represent another research area that could be applied for designing antennas with multiple resonances [23, 24].

The rest of this paper is organized as follows. In Sect. 2 inductive coupling fundamentals are revisited. In Sect. 3 the two strategies of maximizing either the *power transfer efficiency* or the *transferred power* are compared. Section 4 describes the results by using scattering parameters. The analysis of load modulation and its impact on bandwidth are presented in Sect. 5, and Sect. 6 gives the conclusions.



## 2 Inductive coupling

Inductive or magnetic coupling between two coils is the basic principle that is described for wireless power transfer and communication below (see Fig. 1). The equivalent circuit for such systems is illustrated in Fig. 2, including source, load, primary and secondary coils and matching networks for the primary and secondary sides. The matching networks are either composed of a series or a parallel capacitance. Figure 2 contains the wave amplitudes  $a_1, b_1, a_2, b_2$  that are referred to later in this paper in order to describe the whole system with a corresponding scattering matrix.

If the two coils are arranged as a transformer with concordant winding and use the current directions introduced in Fig. 2 (symmetric reference arrows), then the relation between the coil voltages and currents is as follows:

$$\begin{bmatrix} U_{L1} \\ U_{L2} \end{bmatrix} = \begin{bmatrix} j\omega L_1 & j\omega M \\ j\omega M & j\omega L_2 \end{bmatrix} \begin{bmatrix} I_1 \\ I_2 \end{bmatrix}. \tag{1}$$

The mutual inductance  $M$  is

$$M = k\sqrt{L_1 L_2}, \tag{2}$$

where  $L_1$  and  $L_2$  are the inductance of the primary and secondary coil, respectively, and  $k$  denotes the coupling factor between these two coils. The coupling factor depends on how the two coils are arranged with respect to each other.

To determine  $k$  by measurement, the voltages directly at the primary and secondary coils need to be determined with  $I_2 = 0$  (secondary coil is open). With (1),  $k$  follows directly as

$$k = \sqrt{\frac{L_1 U_{L2}}{L_2 U_{L1}}}. \tag{3}$$

Alternatively, the resulting inductance  $L_S$  can be measured when the secondary coil is shorted ( $U_{L2} = 0$ ) [25]. Then,  $k$  follows as

$$k = \sqrt{1 - \frac{L_S}{L_1}}. \tag{4}$$

Using electromagnetic field theory,  $L_1$ ,  $L_2$ ,  $M$  and, thus,  $k$  can be determined analytically [26, 27]. For circular coils with only a few windings that are concentric and parallel with distance  $d$  as in Fig. 1 the following approximations can be used [26]:

$$L_i \approx N_i^2 \mu_0 \rho_i \left( \ln \left( \frac{8\rho_i}{r_0} \right) - \frac{7}{4} \right), \quad i = 1, 2, \tag{5}$$

$$M \approx N_1 N_2 \frac{\mu_0 \pi}{2} \frac{\rho_1^2 \rho_2^2}{(d^2 + (\rho_1 + \rho_2)^2)^{3/2}}. \tag{6}$$

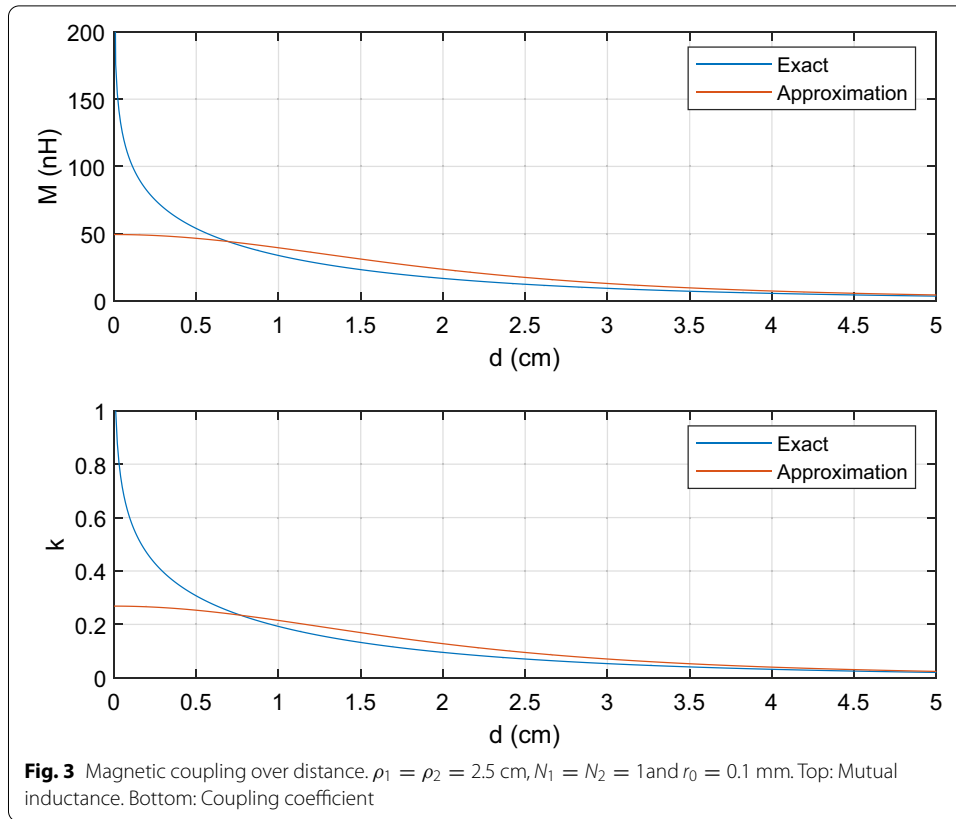
The radii of the two coils are denoted by  $\rho_1$  and  $\rho_2$ ;  $N_1$  and  $N_2$  are the windings of the two coils. The parameter  $r_0$  denotes the radius of the wire of which the coils are constructed, and  $\mu_0$  is the permeability of free space. For these approximations, thin wires and coil configurations with one radius much larger than the other are assumed. The resulting coupling factor over distance  $d$  is depicted for  $\rho_1 = \rho_2 = 2.5$  cm,  $N_1 = N_2 = 1$  and  $r_0 = 0.1$  mm in Fig. 3. Here, the exact results based on electromagnetic field analysis as well as approximations based on (5) and (6) are shown. As seen, the approximation only approaches the exact results for high  $k$  because the assumption of different coil radius does not hold.

In the following derivation of the optimization criteria, the quality factors

$$Q_1 = \frac{\omega L_1}{R_1} \text{ and } Q_2 = \frac{\omega L_2}{R_2} \tag{7}$$

will be of importance. The resistances  $R_1$  and  $R_2$  describe the ohmic losses of the two coils. From basic circuit theory, the relation of all voltages, currents and component parameters can now be written as

$$\begin{bmatrix} U_0 - I_1 R_0 \\ -I_L R_L \end{bmatrix} = \begin{bmatrix} Z_{11} & Z_{12} \\ Z_{21} & Z_{22} \end{bmatrix} \begin{bmatrix} I_0 \\ I_L \end{bmatrix}, \tag{8}$$



which can be rewritten for series capacitance on the primary as well as the secondary side as

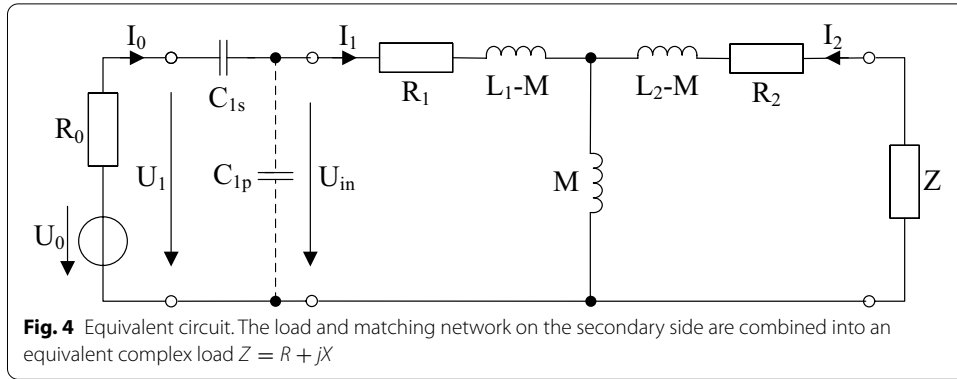
$$\begin{bmatrix} U_0 - I_0 R_0 \\ -I_2 Z \end{bmatrix} = \begin{bmatrix} R_1 + j\omega L_1 + \frac{1}{j\omega C_{1s}} & j\omega M \\ j\omega M & R_2 + j\omega L_2 + \frac{1}{j\omega C_{2s}} \end{bmatrix} \begin{bmatrix} I_1 \\ I_2 \end{bmatrix}. \tag{9}$$

Here, the load resistance  $R_L$  and the matching network on the secondary side are combined to a complex load  $Z = R + jX$ .

The analysis of the power transfer and efficiencies below uses the equivalent circuit in Fig. 4. The total impedance seen at the first coil can be derived as

$$\begin{aligned} Z_{in} &= \frac{U_{in}}{I_1} = R_1 + j\omega L_1 + \frac{\omega^2 M^2}{R_2 + R + j(\omega L_2 + X)} \\ &= R_1 + \frac{\omega^2 M^2 (R_2 + R)}{(R_2 + R)^2 + (\omega L_2 + X)^2} + j \left( \omega L_1 - \frac{\omega^2 M^2 (\omega L_2 + X)}{(R_2 + R)^2 + (\omega L_2 + X)^2} \right). \end{aligned} \tag{10}$$

This is analogous to [28]. Depending on whether series or parallel matching is applied on the secondary side, the basic relations between  $Z = R + jX$  and components  $R_L$ ,  $C_{2s}$  and  $C_{2p}$  need to be considered (see Fig. 2).



Series matching on the secondary side:

$$R = R_L, \quad X = \frac{-1}{\omega C_{2s}}. \tag{11}$$

Parallel matching on the secondary side:

$$R = \frac{R_L}{(\omega C_{2p} R_L)^2 + 1}, \quad X = \frac{-\omega C_{2p} R_L^2}{(\omega C_{2p} R_L)^2 + 1}, \tag{12}$$

$$R_L = R + \frac{1}{(\omega C_{2s})^2 R}, \quad \omega C_{2p} = \frac{-X}{R^2 + X^2}. \tag{13}$$

This holds for all derivations in what follows so that the differentiation between these two cases will not be repeated every time. With the relation between the two currents

$$I_2 = \frac{j\omega M}{R_2 + j\omega L_2 + R + jX} I_1, \tag{14}$$

the active power provided to the load on the secondary side follows as

$$P_2 = |I_2|^2 R = |I_1|^2 \frac{\omega^2 M^2 R}{(R_2 + R)^2 + (\omega L_2 + X)^2}. \tag{15}$$

The total active power provided to the primary side is

$$\begin{aligned} P_1 &= |I_1|^2 R_1 + |I_2|^2 (R_2 + R) \\ &= |I_1|^2 \left( R_1 + \Re \left\{ \frac{j\omega M (j\omega (L_2 - M) + R_2 + R + jX)}{j\omega L_2 + R_2 + R + jX} \right\} \right) \\ &= |I_1|^2 \left( R_1 + \frac{\omega^2 M^2 (R_2 + R)}{(R_2 + R)^2 + (\omega L_2 + X)^2} \right). \end{aligned} \tag{16}$$

In [2], two additional power parameters are analyzed in order to emphasize the difference between a classical transformer ( $k \approx 1$ ) and wireless coupling with low coupling factors ( $k < 0.5$ ). First, the active power transferred to the secondary side is

$$P_{12} = |I_2|^2(R_2 + R) = |I_1|^2 \frac{\omega^2 M^2 (R_2 + R)}{(R_2 + R)^2 + (\omega L_2 + X)^2}, \tag{17}$$

where the difference compared to  $P_2$  is the additional resistor  $R_2$  in the numerator. Furthermore, the reactive power that goes into the coil system is given as

$$\begin{aligned} Q_{12} &= |I_1|^2 \omega (L_1 - M) + |I_2|^2 (L_2 - M) + |I_1 + I_2|^2 \omega M \\ &= |I_1|^2 \left( \omega L_1 + \Im \left\{ \frac{j\omega M (j\omega (L_2 - M) + R_2 + R + jX)}{j\omega L_2 + R_2 + R + jX} \right\} \right) - |I_2|^2 X \\ &= |I_1|^2 \left( \omega L_1 - \frac{\omega^2 M^2 (\omega L_2 + 2X)}{(R_2 + R)^2 + (\omega L_2 + X)^2} \right). \end{aligned} \tag{18}$$

For a traditional transformer, the reactive power represents the magnetizing power, where higher magnetizing power brings higher copper and core loss [2]. Therefore, the ratio of active to reactive power should be maximized in this case (see next section).

### 3 Optimization criteria

#### 3.1 Power transfer efficiency

For optimizing magnetic coupling systems, different criteria have been proposed. The power transfer efficiency (PTE) is defined as [2, 3]

$$\begin{aligned} \text{PTE} &= \frac{P_{\text{out}}}{P_{\text{in}}} = \frac{P_2}{P_1} = \frac{|I_2|^2 R_L}{|I_1|^2 R_1 + |I_2|^2 R_2 + |I_2|^2 R_L} \\ &= \frac{\omega^2 M^2 R}{R_1 ((R_2 + R)^2 + (\omega L_2 + X)^2) + \omega^2 M^2 (R_2 + R)}. \end{aligned} \tag{19}$$

Maximizing the PTE refers to achieving energy efficiency with minimum system losses. These losses arise from ohmic losses in the coils. The first condition for maximizing the PTE is to completely remove the imaginary impedance part on the secondary side of the WPT system. That is,  $\omega_0 L_2 = -X$ , with  $\omega_0$  being the angular frequency at resonance, resulting in

$$\text{PTE}_{\text{max}} = \frac{\omega_0^2 M^2 R}{R_1 (R_2 + R)^2 + \omega_0^2 M^2 (R_2 + R)}. \tag{20}$$

However, the first condition  $\omega_0 L_2 = -X$  has an impact on maximizing the PTE only if  $R_1 L_2^2 > M^2 (R_2 + R)$ . This holds for loosely coupled coils, which are the focus of this paper. For a classical transformer with  $k \approx 1$ , this does not hold so a matching circuit is not of interest. Moreover, the efficiency of a classical transformer also suffers from losses due to a high reactive power as in (18). When maximizing the ratio of active power in (17) to reactive power in (18) with  $k = 1$ , the imaginary impedance part  $X$  on the secondary side must be  $X = 0$ . In the following, loosely coupled coils are considered, and we assume that  $X = -\omega_0 L_2$ .

The second condition for maximizing the PTE can be derived as [2]

$$R = \sqrt{R_2^2 + \omega_0^2 M^2 \frac{R_2}{R_1}} = R_2 \sqrt{1 + k^2 Q_1 Q_2}. \tag{21}$$

Depending on the chosen matching option on the secondary side,  $R_L$ ,  $C_{2s}$  or  $C_{2p}$  can be determined according to (11) and (13). That is, for a series-compensated secondary side,  $R_L$  and  $C_{2s}$  follow directly from (11):  $R_L = R$  and  $\omega_0 C_{2s} = 1/(\omega_0 L_2)$ . For a parallel-compensated secondary side,  $R_L$  and  $C_{2p}$  need to be calculated according to (13). In particular, for a low coupling coefficient  $k$ ,  $R$  for maximizing PTE in (21) becomes small with  $R \approx R_2$ . So, the series-compensated secondary is well suited for applications with a small load resistance  $R_L = R$ , whereas a much higher optimal load resistance  $R_L$  results for the parallel-compensated secondary side according to (13). In other words, for a given load resistance  $R_L$ , a series-compensated secondary side can provide a stable voltage, whereas a parallel-compensated secondary side is able to supply a stable current [29].

For an example scenario with the parameters given in Table 1, Fig. 5 shows the maximum achievable PTE over different coupling factors  $k$ . Figure 6 shows the PTE over the coupling factor  $k$  and resistance  $R$  for a constant frequency  $f_0 = 13.56$  MHz. All other simulation parameters are set according to Table 1.

### 3.2 Transferred power

For the PTE, matching between the source and the coil system does not need to be considered. In contrast to that, the transferred power (TP) is defined as [3]

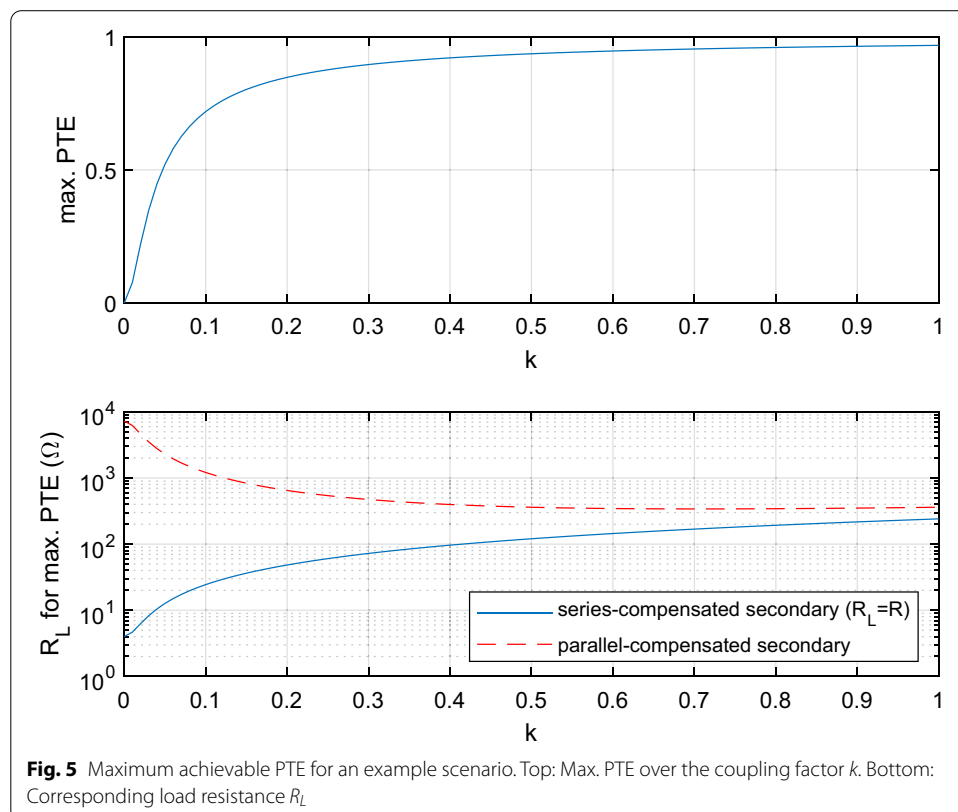
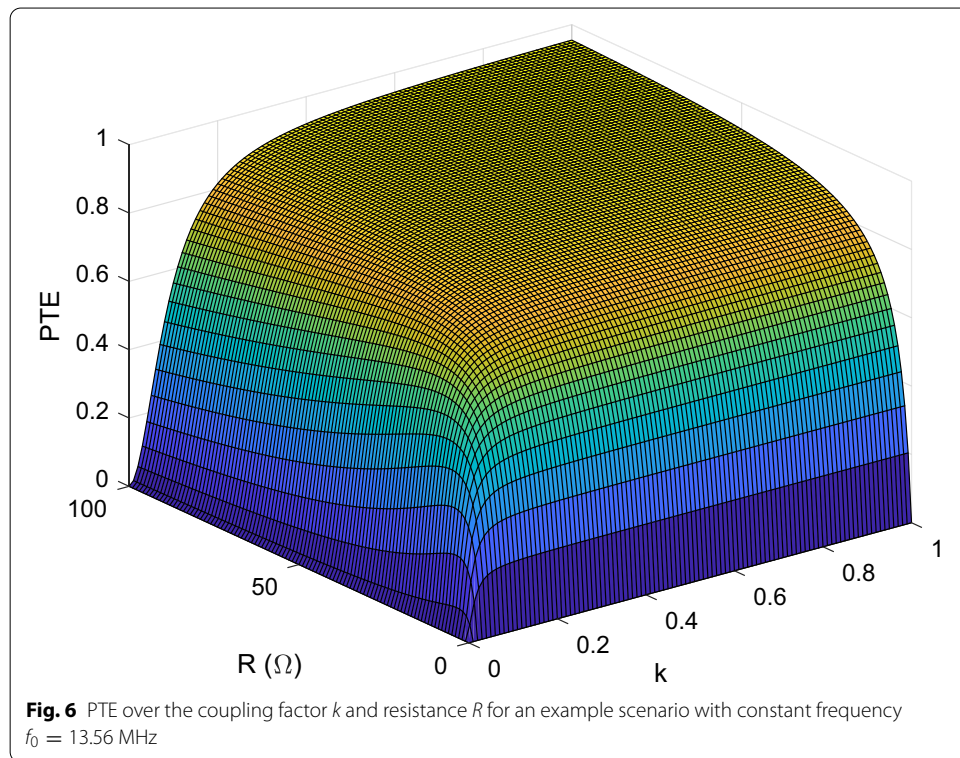


**Table 1** Simulation parameters

Component	Value
$f_0$	13.56 MHz
$L_1$	3 $\mu$ H
$L_2$	2 $\mu$ H
$R_1$	3 $\Omega$
$R_2$	4 $\Omega$
$R_0$	50 $\Omega$



$$TP = \frac{P_{out}}{P_{available}} = \frac{|I_2|^2 R}{|U_0|^2 / (4R_0)} \tag{22}$$

Here, the output power at the load is normalized to the available source power. Thus, the mismatch between the source and the remaining network is taken into account.

For finding the optimized matching components and load resistance, partial optimization of the network obtained from PTE maximization is assumed in what follows. That is, the first condition for PTE maximization  $\omega_0 L_2 = -X$  also holds for TP maximization. However, the optimal load resistance  $R_L$  is different here than in (21). Moreover, a matching network consisting either of  $C_{1s}$  or  $C_{1p}$  needs to be found.

### 3.2.1 Series-compensated primary side

In the first case, using the series capacitor  $C_{1s}$  on the primary side, matching follows directly by first satisfying  $\omega_0 L_1 = \frac{1}{\omega_0 C_{1s}}$ , resulting in

$$TP_{\max} = \frac{4R_0\omega_0^2 M^2 R}{((R_0 + R_1)(R_2 + R) + \omega_0^2 M^2)^2} \tag{23}$$

Maximizing TP is achieved with

$$R = R_2 + \frac{\omega_0^2 M^2}{R_0 + R_1}, \tag{24}$$

and the load resistance and matching components are obtained according to (11) and (13). This result for series matching on the primary as well as secondary side was also shown in [30].

### 3.2.2 Parallel-compensated primary side

With parallel matching on the primary side, the derivation of the optimal  $C_{1p}$  aims at compensating the imaginary part of  $Z_{in}$  in (10) while maximizing the transferred power:

$$\omega_0 C_{1p} = \frac{\omega_0 L_1}{\left(\frac{\omega_0^2 M^2}{R_2 + R} + R_1\right)^2 + (\omega_0 L_1)^2} \tag{25}$$

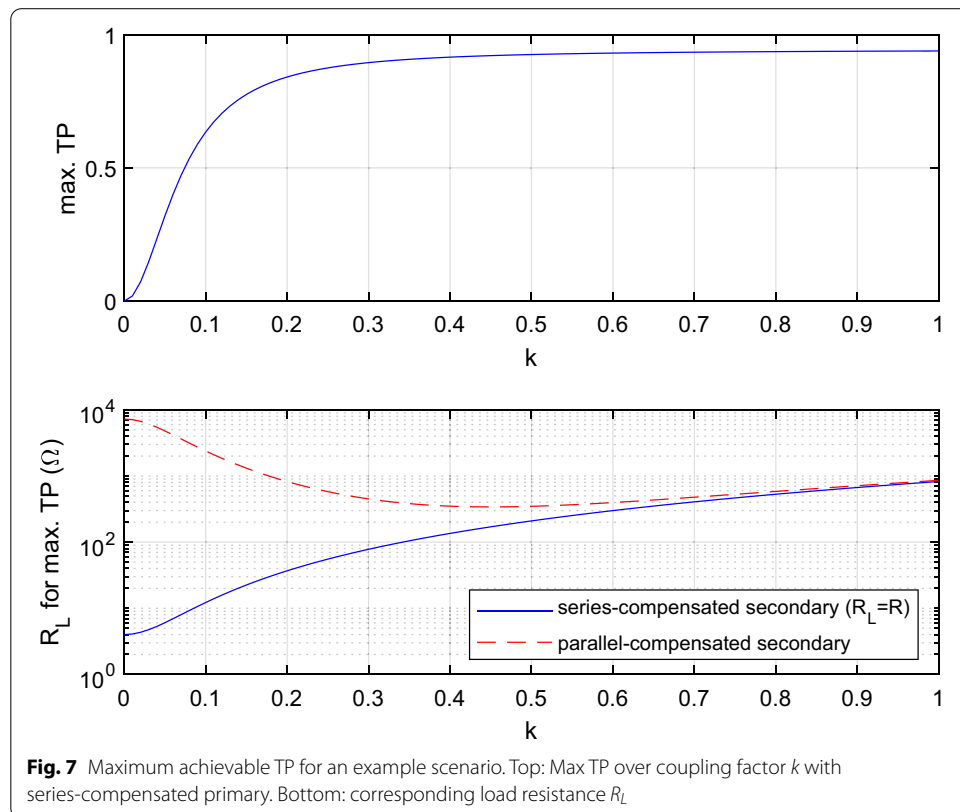
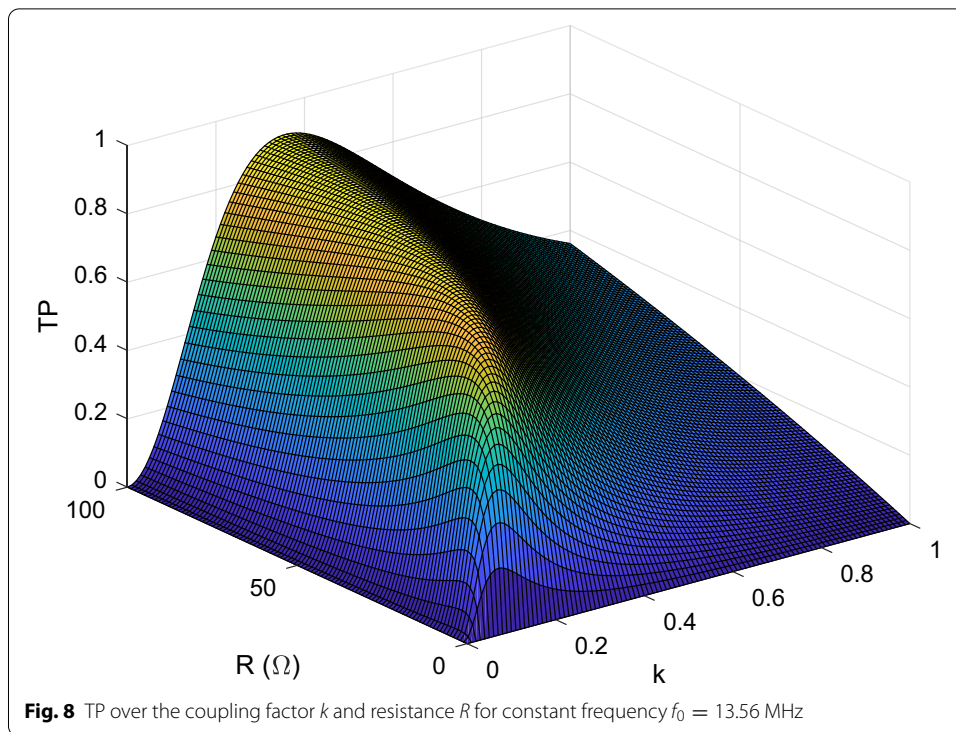


**Fig. 7** Maximum achievable TP for an example scenario. Top: Max TP over coupling factor  $k$  with series-compensated primary. Bottom: corresponding load resistance  $R_L$



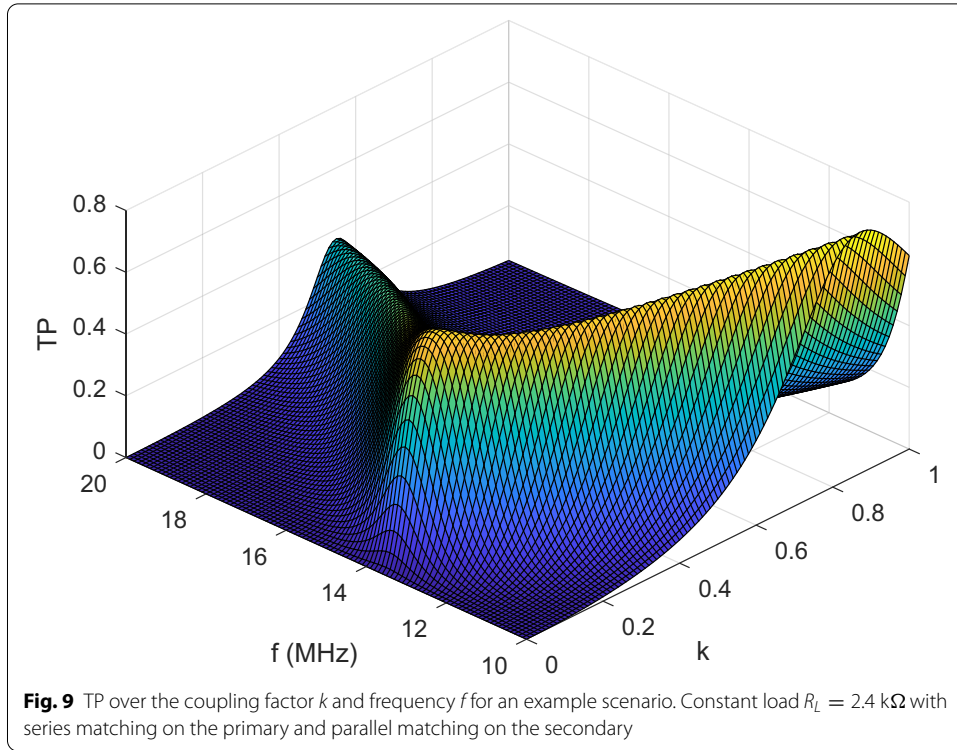
The derivation of the optimal load resistance is now different than in the previous case since  $C_{1p}$  and  $R$  depend on each other.

For the example scenario with the simulation parameters given in Table 1, Fig. 7 shows the maximum achievable TP for different coupling factors  $k$ .

If matching on the primary side is not sufficient, additional means can be added in order to match the overall impedance seen at port 1 to the source impedance  $R_0$ , but then the closed-form expression in (24) does not apply. One option is to combine a series and a parallel capacitor. Alternatively, we could add another inductor in series with the source. Inductance in series with the source could also be achieved by connecting the capacitor in parallel to only a part of the coil. Thus, the inductance of the coil would be separated into a parallel and a series part, which is largely a trial-and-error method.

In [29], a slightly different matching strategy is followed than the one in this paper. There, the matching capacitor on the secondary side is always directly related to the secondary inductance, regardless of whether it is applied in series or in parallel:  $\omega_0 L_2 = \frac{1}{\omega_0 C_{2s}} = \frac{1}{\omega_0 C_{2p}}$ . This results in a remaining imaginary impedance part on the secondary side for the parallel case. On the primary side, the remaining imaginary component is compensated by using either  $C_{1s}$  or  $C_{1p}$ , which results in the same values as in this paper. For parallel matching on the secondary side, the matching is different on the primary side.

Figure 8 shows the TP over the coupling factor  $k$  and resistance  $R$  for a constant frequency  $f_0 = 13.56$  MHz. Figure 9 shows the TP over the coupling factor  $k$  and frequency  $f$  for a constant load  $R_L = R = 2.4$  k $\Omega$  with a series-compensated primary and parallel-compensated secondary. All other simulation parameters are set according to Table 1.



The formulas for the PTE and TP, in combination with the figures based on the specific simulation parameters in Table 1, show the dependencies between the different system parameters. When we reduce, for example, coil losses by using lower values for  $R_1$  and  $R_2$  compared to the values in Table 1, the PTE and TP can increase; however, this is only true if the coupling coefficient and load resistance are adapted. The range for such adapted parameters can become very small. That is, a lossless coil in combination with the wrong load resistance might result in worse PTE and TP than for a lossy coil. Likewise, coils with high inductance obviously offer good magnetic coupling; however, if the coupling coefficient  $k$  is high at the same time, the load resistance needs to be high enough to take advantage of good coupling.

#### 4 Scattering parameters

Using scattering parameters (S-parameters), which is a useful method for experimental prototype evaluation with network analyzers, we obtain the relationships between the wave amplitudes in Fig. 2 via the scattering matrix  $S$ :

$$\begin{bmatrix} b_1 \\ b_2 \end{bmatrix} = \begin{bmatrix} S_{11} & S_{12} \\ S_{21} & S_{22} \end{bmatrix} \begin{bmatrix} a_1 \\ a_2 \end{bmatrix} = S \begin{bmatrix} a_1 \\ a_2 \end{bmatrix}, \tag{26}$$

with

$$a_2 = b_2 r_L, \quad r_L = \frac{R_L - R_{02}}{R_L + R_{02}}, \quad b_2 = \frac{a_1 S_{21}}{1 - r_L S_{22}}. \tag{27}$$

Moreover,  $R_{02}$  is the characteristic impedance of the two-port network at port 2. At port 1, the characteristic impedance is usually assumed to be  $R_{01} = R_0$  unless denoted otherwise. The outgoing wave at port 1 can then be written as

$$b_1 = a_1 S_{11} + a_2 S_{12} = a_1 \left( S_{11} + \frac{r_L S_{12} S_{21}}{1 - r_L S_{22}} \right) = a_1 r_1. \quad (28)$$

For the optimization criteria, it then follows that

$$\text{PTE} = \frac{\frac{1}{2}(|b_2|^2 - |a_2|^2)}{\frac{1}{2}(|a_1|^2 - |b_1|^2)} = \frac{|S_{21}|^2(1 - |r_L|^2)}{|1 - r_L S_{22}|^2(1 - |r_1|^2)}, \quad (29)$$

$$\text{TP} = \frac{\frac{1}{2}(|b_2|^2 - |a_2|^2)}{\frac{1}{2}|a_1|^2} = \frac{|S_{21}|^2(1 - |r_L|^2)}{|1 - r_L S_{22}|^2}. \quad (30)$$

For the reflection coefficient  $r_L = 0$ , these expressions simplify to

$$\text{PTE} = \frac{|S_{21}|^2}{1 - |S_{11}|^2}, \quad (31)$$

$$\text{TP} = |S_{21}|^2. \quad (32)$$

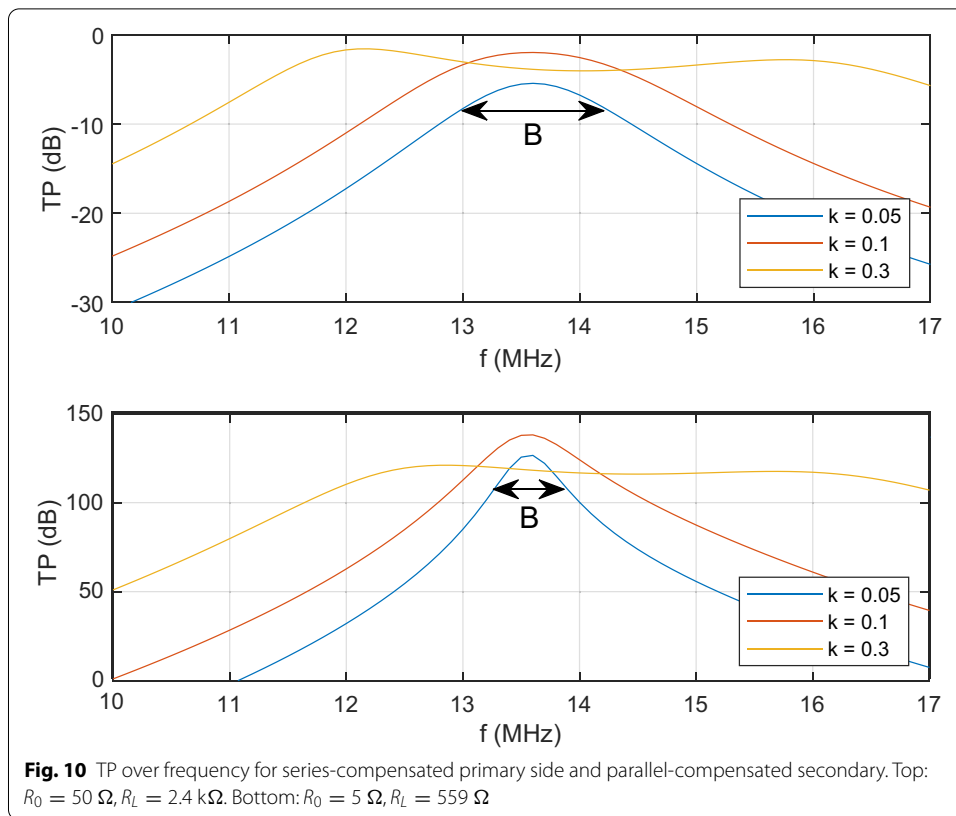
In this case, the characteristic impedance equals the load impedance at port 2:  $R_{02} = R_L$ . For theoretical or simulation-based treatments of WPT systems, this assumption can be made easily. However, when carrying out measurements with a network analyzer, one is typically restricted to  $R_{01} = R_{02} = 50 \Omega$ . Then, the PTE and TP can be determined with (29) and (30) and the measured S-parameters.

Moreover, the S-parameters in (26) can be converted into the two-port network parameters in impedance form in (8) and vice versa [31].

## 5 Bandwidth

### 5.1 General considerations

Returning to the TP depicted with respect to frequency in Fig. 9, we now focus on the bandwidth of the inductively coupled communication system. The bandwidth  $B$  is usually defined as the *half-power bandwidth*, where the transmission response is 3 dB lower than at resonance [31]. Figure 10 shows TP over frequency for three selected coupling coefficients. The bandwidth  $B$  is illustrated for the example coupling coefficient  $k = 0.05$ . The upper figure shows the results for the simulation parameters that have been used up to now; for the lower figure, the source resistance is changed to  $R_0 = 5 \Omega$  and the adapted load resistance  $R_L = 559 \Omega$  is optimized again according to (24) and (13). For strong coupling with  $k = 0.3$ , we can also see in Fig. 10 the two resonances that were shown previously in Fig. 9. Extending the bandwidth definition to a 3 dB reduction compared to the maximum (instead of a single resonance), it can be seen that the bandwidth depends greatly on the coupling coefficient (here, a high bandwidth is obtained for  $k = 0.3$ ) and all other system parameters and not just, for example, on the bandwidth of the RFID tag, which is treated as a simple parallel resonance circuit [31]:



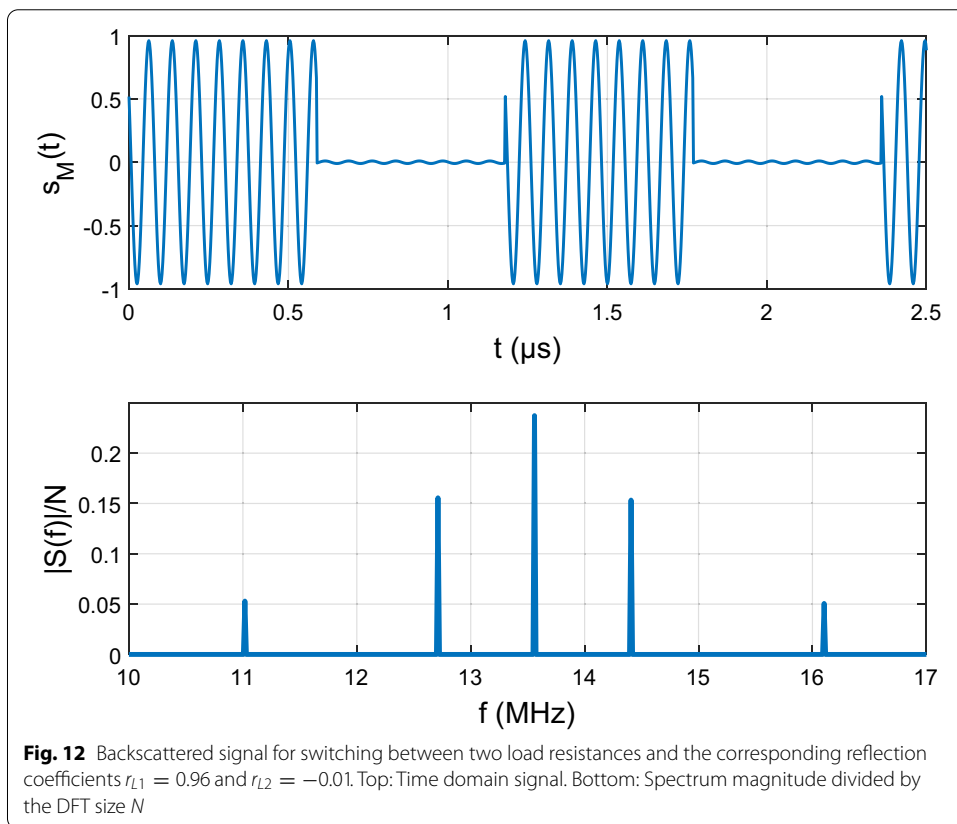
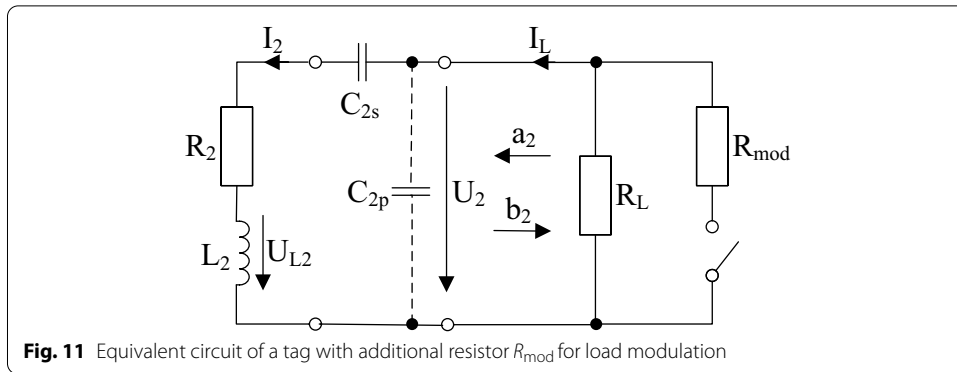
$$B_{\text{tag}} = \frac{f_0}{Q} = \frac{2\pi f_0^2 L_2}{R_L}, \tag{33}$$

where  $Q$  is the quality factor of the tag.

For data transmission, the bandwidth is directly related to the data rate. With a data rate of, for example, 106 kbit/s and binary modulation in an RFID system,  $B = 106 \text{ kHz}$  would be required. This holds true for data transfer from an RFID reader to a tag. High bandwidth is of importance because this leads to short time constants and less interference between consecutively transmitted bits in the time domain [8]. For the other direction, from tag to reader, data transmission is usually based on load modulation at the transponder side. In higher-frequency systems operating at 6.78 or 13.56 MHz, the transponder’s load modulator is controlled by a modulated subcarrier signal. The subcarrier frequency  $f_i$  can be 847 kHz (ISO 14443-2) or 423 kHz (ISO 15693) [10]. However, a high bandwidth  $B$  does not directly describe the frequency characteristics of the information-containing sidebands. These sidebands may even lie outside the bandwidth, indicating the 3 dB damping around the carrier frequency. However, a low  $Q$  and, thus, high  $B$  still indicates more or less flat frequency characteristics.

### 5.2 Load modulation

In what follows, sideband generation by means of switching between different load resistances in an RFID tag is examined. This is similar to the treatment in [13], where



load modulation for UHF RFID systems is analyzed. There, sidebands are generated by switching between two different complex-valued RCSs of the tag antenna. The switching process is treated as a subcarrier signal with a certain frequency. The tag information is then carried by the subcarrier and appears as sidebands in the spectrum. So, the sideband power is of interest here. For inductive coupling, the focus of this paper, Fig. 11 shows an example of load modulation performed by switching between different load resistances [10]. That is, an additional resistor  $R_{mod}$  is switched in parallel to the existing load  $R_L$  at a certain frequency.

For an illustration of backscatter modulation and subcarrier generation, Fig. 12 shows an example: a  $f_0 = 13.56$  MHz carrier signal simulating an incoming voltage from an

RFID reader observes an amplitude and phase modulation by a subcarrier with a frequency of  $f_0/16 = 847.5$  kHz. This modulated signal sends a backscattered signal back to the RFID reader.

The two sidebands of the backscattered signal at  $f_0 + 847.5$  kHz and  $f_0 - 847.5$  kHz in Fig. 12 contain the required information of an RFID tag. For simplicity, in the aforementioned figures as well as in those below, additional modulation of the subcarrier with an identification number (ID) or any sensor value is not shown here. Such modulation would cause further spectral lines around the sidebands.

The mathematical description of the backscattered signal and the sideband power can be obtained as follows: The incident complex wave amplitude at the load resistance of an RFID tag is  $a_1 S_{21}$ , which is defined in the frequency domain. For the derivation of the sidebands, we now define a time-domain signal

$$s_c(t) = \Re\{a_1 S_{21} e^{j\omega_0 t}\}. \tag{34}$$

We assume here for simplicity that  $a_1$  and  $S_{21}$  are real-valued, which results in

$$s_c(t) = a_1 S_{21} \cos(\omega_0 t). \tag{35}$$

Switching between different load resistances values can be seen as an information-containing signal

$$s_i(t) = r_L(t) = \frac{r_{L1} + r_{L2}}{2} + \frac{2}{\pi}(r_{L1} - r_{L2}) \left( \sin(\omega_i t) + \frac{1}{3} \sin(3\omega_i t) + \frac{1}{5} \sin(5\omega_i t) + \dots \right). \tag{36}$$

That is,  $r_L(t)$  describes a rectangular signal toggling between the values  $r_{L1}$  and  $r_{L2}$  as the subcarrier.

The backscattered signal follows as modulation of the carrier signal with the subcarrier. The real-valued bandpass version of the backscattered signal is

$$s_M(t) = a_1 S_{21} \Re\{s_i(t) e^{j\omega_0 t}\} = a_1 S_{21} \Re\{s_i(t)\} \cos(\omega_0 t) - a_1 S_{21} \Im\{s_i(t)\} \sin(\omega_0 t), \tag{37}$$

where  $\Re\{\cdot\}$  and  $\Im\{\cdot\}$  denote the real and imaginary parts of its argument, respectively. Using trigonometric functions and neglecting the higher frequency parts in (36), such as  $3\omega_i, 5\omega_i$ , we obtain

$$\begin{aligned} s_M(t) &= \frac{a_1 S_{21}}{2} (\Re\{r_{L1} + r_{L2}\} \cos(\omega_0 t) - \Im\{r_{L1} + r_{L2}\} \sin(\omega_0 t)) \\ &\quad + \frac{a_1 S_{21}}{\pi} \Re\{r_{L1} - r_{L2}\} (\sin((\omega_0 + \omega_i)t) - \sin((\omega_0 - \omega_i)t)) \\ &\quad + \frac{a_1 S_{21}}{\pi} \Im\{r_{L1} - r_{L2}\} (\cos((\omega_0 + \omega_i)t) - \cos((\omega_0 - \omega_i)t)). \end{aligned} \tag{38}$$

The backscattered signal power for one of the two frequencies  $\omega_0 + \omega_i$  and  $\omega_0 - \omega_i$ , corresponding to the two sidebands in the example in Fig. 12, follows as

$$\begin{aligned}
 P_M &= \frac{a_1^2 S_{21}^2}{2\pi^2} \left( \Re\{r_{L1} - r_{L2}\}^2 + \Im\{r_{L1} - r_{L2}\}^2 \right) \\
 &= \frac{a_1^2 S_{21}^2}{2\pi^2} |r_{L1} - r_{L2}|^2 = \frac{2}{N^2} |S(\omega_0 + \omega_i)|^2 = \frac{2}{N^2} |S(\omega_0 - \omega_i)|^2,
 \end{aligned} \tag{39}$$

where  $N$  is the size of the discrete Fourier transform (DFT)  $S(\omega)$ . This important result shows the relation between different reflection coefficients in an RFID tag due to different load resistances and signal power.

Using the information from the time-domain signal representation in (38), we can now return to the frequency-domain analysis using scattering parameters. First, the modulated signal in the frequency domain is generally

$$s_M(f) = a_1 S_{21} r_L(f). \tag{40}$$

From (38), three different reflection coefficients can then be derived for the carrier and two sideband signals:

$$\begin{aligned}
 r_{L0} &= \frac{1}{2}(r_{L1} + r_{L2}), \\
 r_{Lup} &= \frac{-j}{\pi}(r_{L1} - r_{L2}), \quad r_{Llo} = \frac{j}{\pi}(r_{L1} - r_{L2}).
 \end{aligned} \tag{41}$$

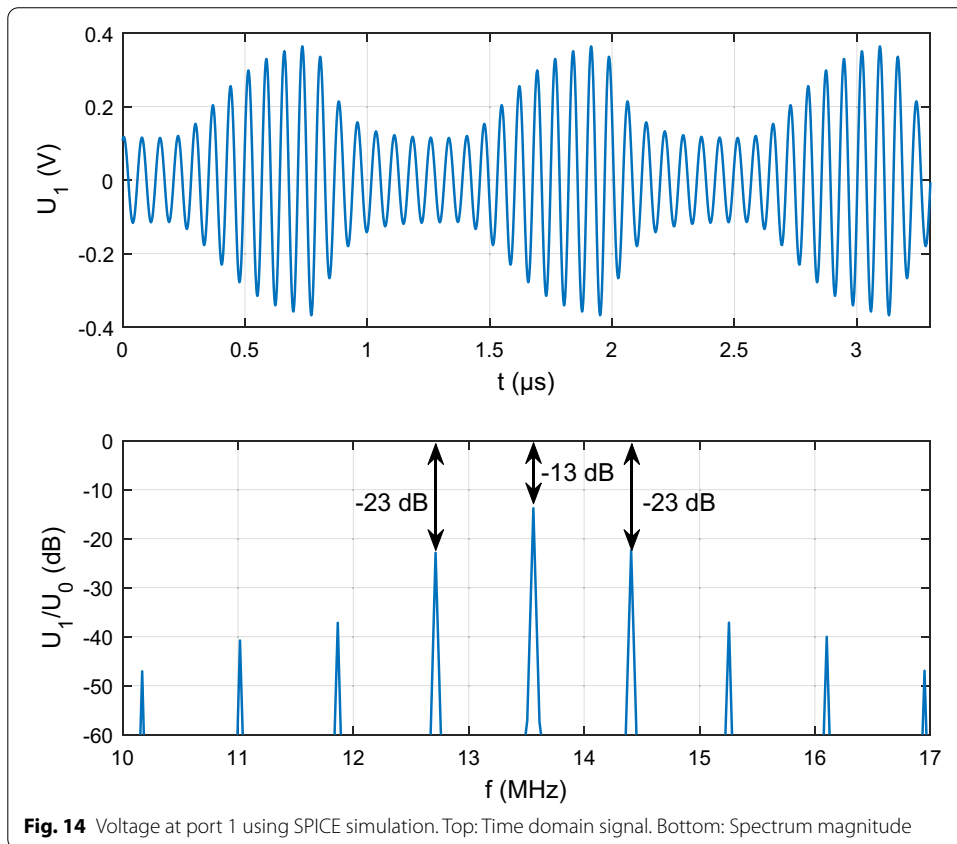
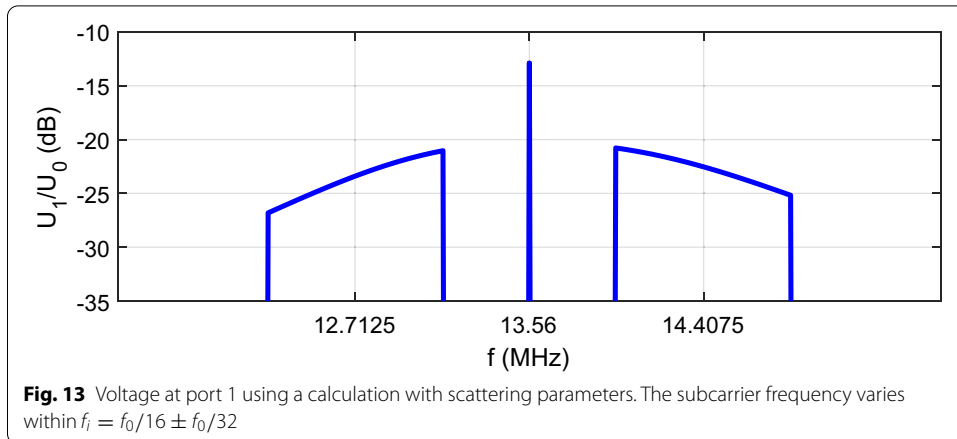
The overall reflected wave at port 1 and port 2 can now be determined using (27) and (28), respectively. However, the frequency dependency ( $f_0, f_0 + f_i$  or  $f_0 - f_i$ ) needs to be considered for the components  $r_L, S_{22}$  and  $S_{12}$ . This, however, is not a typical usage of scattering parameters because they are defined for a single frequency in a steady-state scenario. In contrast, the time dependency of the reflection coefficient causes new frequency components that are reflected at port 2 (described by  $S_{22}$ ) and so forth. To use the scattering parameter approach, we make use of a reference impedance  $R_{02} = R_L$  at port 2 in order to ensure  $S_{22}$  negligibly small. Then, the terms in (27) and (28) can be simplified by setting  $S_{22} = 0$ . Finally, the complex-valued voltage amplitude at port 1, which is

$$U_1 = \sqrt{R_0}(a_1 + b_1) = \sqrt{R_0}a_1 \left( 1 + \frac{b_1}{a_1} \right) = \frac{U_0}{2} \left( 1 + \frac{b_1}{a_1} \right) \tag{42}$$

can be written for the three frequency components – the carrier frequency and the two sidebands – as

$$\begin{aligned}
 U_1(f_0) &= \frac{U_0(f_0)}{2} (1 + S_{11}(f_0) + S_{21}(f_0)S_{12}(f_0)r_{L0}), \\
 U_1(f_0 + f_i) &= \frac{U_0(f_0)}{2} S_{21}(f_0)S_{12}(f_0 + f_i)r_{Lup}, \\
 U_1(f_0 - f_i) &= \frac{U_0(f_0)}{2} S_{21}(f_0)S_{12}(f_0 - f_i)r_{Llo}.
 \end{aligned} \tag{43}$$

Figure 13 illustrates the voltage at port 1 in relation to the source voltage for a scenario using the simulation parameters in Table 1. Moreover, further parameters for optimizing the TP using series matching at the primary and parallel matching at the secondary side are:  $k = 0.1, C_{1s} = 46$  pF,  $C_{2p} = 68$  pF,  $R_L = 2.4$  kΩ and  $R_{mod} = 50$  Ω. As we



can see, the voltage at port 1 changes while varying the subcarrier frequency  $f_i$ . This is done here in order to illustrate the frequency characteristics that a signal modulated to the subcarriers would face. The frequency characteristics of the scattering parameter  $S_{12}(f)$  cause the amount of distortion in the sideband signals to be transferred from the tag to the RFID reader. However, it is noteworthy again here that it is not the bandwidth

directly around the carrier but that around the subcarrier that is of interest for the communication from tag to reader.

For the same scenario, Fig. 14 shows the results using a SPICE simulation. As seen, the carrier and subcarrier voltages match those from the scatter parameter calculation (with a tolerance of approximately 0.5 dB).

As mentioned in the introduction, the wavelet transformation can be used here for signal analysis as well. For example, Morse or Morlet wavelets [22] would provide frequency information with additional resolution in time. Scaling the wavelets to be narrow in time yields peaks at the transition between the two switching states in Fig. 12, which are proportional to the backscattered signal power in (39).

## 6 Conclusion

A method of maximizing the transferred power between two inductively coupled coils was described. This is of interest for wireless power transfer and was highlighted in this paper for RFID and NFC. For communication and data transfer in RFID/NFC, signal distortion due to frequency-selective transfer characteristics is also an issue. To take this into account, the system model for inductively coupled coils was extended by load modulation and its description in the time and frequency domains. For this purpose, the subcarrier power at an RFID reader due to load modulation at a tag was derived using scattering parameters.

### Abbreviations

NFC: Near-field communication; RFID: Radio-frequency identification; WPT: Wireless power transfer; IPT: Inductive power transfer; HF: High frequency; ISM: Industrial, scientific and medical; RF: Radio frequency; RCS: Radar cross section; PTE: Power transfer efficiency; TP: Transferred power.

### Acknowledgements

Not applicable.

### Authors' contributions

CD carried out this work and wrote the manuscript. The author read and approved the final manuscript.

### Funding

Open Access funding enabled and organized by Projekt DEAL.

### Availability of data and materials

Not applicable

## Declarations

### Ethics approval and consent to participate

Not applicable

### Competing interests

The authors declare that they have no competing interests.

Received: 23 November 2020 Accepted: 21 April 2021

Published online: 10 May 2021

## References

1. M.P. Kesler, Highly Resonant Wireless Power Transfer: Safe, Efficient, and over Distance (2013). <http://large.stanford.edu/courses/2016/ph240/surakitbovom1/docs/kesler.pdf>. Accessed 14 November 2020
2. S. Li, C.C. Mi, Wireless power transfer for electric vehicle applications. *IEEE Trans. Emerg. Sel. Topics Power Electron.* **3**, 4–17 (2015)
3. J.P.K. Sampath, A. Alphones, Figure of merit for the optimization of wireless power transfer system against misalignment tolerance. *IEEE Trans. Power Electron.* **32**, 4359–4369 (2017)

4. K.N. Mude, Wireless power transfer for electric vehicle. PhD thesis, University of Padova, Italy (2015). <https://core.ac.uk/download/pdf/145233488.pdf>. Accessed 14 November 2020
5. Wireless Power Consortium: The Wireless Power Consortium. <https://www.wirelesspowerconsortium.com>. Accessed 14 November 2020
6. AirFuel Alliance: The AirFuel Alliance. <https://airfuel.org>. Accessed 14 November 2020
7. S. Kim, R. Vyas, J. Bito, K. Niotaki, A. Collado, A. Georgiadis, M.M. Tentzeris, Ambient RF energy-harvesting technologies for self-sustainable standalone wireless sensor platforms. *Proc. IEEE* **102**(11), 1649–1666 (2014)
8. A. Lazaro, R. Villarino, D. Girbau, A survey of NFC sensors based on energy harvesting for IoT applications. *Sensors* **18**(11), 3746 (2018)
9. H. Kim, H. Hirayama, S. Kim, K.J. Han, R. Zhang, J. Choi, Review of near-field wireless power and communication for biomedical applications. *IEEE Access* **5**, 21264–21285 (2017)
10. K. Finkensteller, *RFID Handbook* (Wiley, Chichester, West Sussex, 2010)
11. J.I. Cairó, J. Bonache, F. Paredes, F. Martín, Reconfigurable system for wireless power transfer (WPT) and near field communications (NFC). *IEEE J. Radio Freq. Identif.* **1**(4), 253–259 (2017)
12. O. Franek, Phasor alternatives to Friis' transmission equation. *IEEE Antennas Wirel. Propag. Lett.* **17**, 90–93 (2018)
13. C. Degen, P. Bosselmann, On complex radar cross section and backscatter modulation efficiency in RFID systems, in *Proceedings of the 14th European Conference on Antennas and Propagation (EuCAP)* (2020)
14. I. Daubechies, *Ten Lectures on Wavelets* (SIAM, Philadelphia, Pennsylvania, 1992)
15. S.G. Mallat, A theory for multiresolution signal decomposition: the wavelet representation. *IEEE Trans. Pattern Anal. Mach. Intell.* **11**, 674–693 (1989)
16. E. Guariglia, S. Silvestrov, Fractional-wavelet analysis of positive definite distributions and wavelets on  $D'(C)$ . in S. Silvestrov, M. Rancić (eds) *Engineering Mathematics II. Springer Proceedings in Mathematics and Statistics* 179, 337–353 (2016)
17. X. Zheng, Y.Y. Tang, J. Zhou, A framework of adaptive multiscale wavelet decomposition for signals on undirected graphs. *IEEE Trans. Signal Process.* **67**(7), 1696–1711 (2019)
18. G. Pucciarelli, Wavelet analysis in volcanology: the case of phlegrean fields. *J. Environ. Sci. Eng. A* **6**, 300–307 (2017)
19. X. Liu, H. Zhang, Y.-M. Cheung, X. You, Y.Y. Tang, Efficient single image dehazing and denoising: An efficient multiscale correlated wavelet approach. *Comput. Vis. Image Underst.* **162**, 23–33 (2017)
20. L. Yang, H. Su, C. Zhong, Z. Meng, H. Luo, X. Li, Y.Y. Tang, Y. Lu, Hyperspectral image classification using wavelet transform-based smooth ordering. *Int. J. Wavelets Multiresolut. Inf. Process.* **17**(6), 1950050 (2019)
21. Y.Y. Tang, *Document Analysis and Recognition with Wavelet and Fractal Theories* (The World Scientific Publishing Co, Singapore, 2012)
22. J.M. Lilly, S.C. Olhede, Higher-order properties of analytic wavelets. *IEEE Trans. Signal Process.* **57**(1), 146–160 (2009)
23. E. Guariglia, Harmonic Sierpinski gasket and applications. *Entropy* **20**(9), 714 (2018)
24. E. Guariglia, Primality, fractality, and image analysis. *Entropy* **21**(3), 304 (2019)
25. R.M. Duarte, G.K. Felic, Analysis of the coupling coefficient in inductive energy transfer systems. *Active and Passive Electron. Compon.* (2014). <https://doi.org/10.1155/2014/951624>
26. M. Leone, *Theoretische Elektrotechnik* (Springer, Wiesbaden, Deutschland, 2018)
27. H. Hirayama, Y. Okuyama, N. Kikuma, K. Sakakibara, A consideration of equivalent circuit of magnetic-resonant wireless power transfer, in *Proceedings of the 5th European Conference on Antennas and Propagation (EuCAP)*, pp. 900–903 (2011)
28. Z.N. Low, R.A. Chinga, R. Tseng, J. Lin, Design and test of a high-power high-efficiency loosely coupled planar wireless power transfer system. *IEEE Trans. Ind. Electron.* **56**, 1801–1812 (2009)
29. C.-S. Wang, O.H. Stielau, G.A. Covic, Design considerations for a contactless electric vehicle battery charger. *IEEE Trans. Ind. Electron.* **52**, 1308–1314 (2005)
30. J. Soler, The role of electromagnetic simulation in wireless charging systems, in *Japan Altair Technology Conference* (2017)
31. D.M. Pozar, *Microwave Engineering* (Wiley, Hoboken, NJ, 2012)

## Publisher's Note

Springer Nature remains neutral with regard to jurisdictional claims in published maps and institutional affiliations.

**Submit your manuscript to a SpringerOpen<sup>®</sup> journal and benefit from:**

- Convenient online submission
- Rigorous peer review
- Open access: articles freely available online
- High visibility within the field
- Retaining the copyright to your article

---

Submit your next manuscript at ► [springeropen.com](https://www.springeropen.com)

---